Check for updates

A light-operated dual-mode method for neuroblastoma diagnosis based on a Tb-MOF: from biometabolite detection to logic devices†

Yanhong Liu, Wenyan Dan and Bing Yan ⓘ *

Exploring simple analytical techniques with high accuracy and reliability to quantify biomolecules is crucial, but it remains a great challenge for disease diagnosis. Since the body fluid concentration of most biological targets usually varies in a rather limited range between normal and pathological states, and most systems are greatly limited by a single mechanism/mode of detection, which makes them susceptible to false positive/negative results. Herein, we successfully synthesized a double-mechanism-driven fluorescent sensor based on a Tb-based metal–organic framework (Tb-DBA), which performs quantitative recognition of urinary vanillylmandelic acid (VMA) as an early pathological signature of neuroblastoma (NEURO) accompanied by two completely different luminescence phenomena in a smaller concentration window by switching the excitation wavelength. Notably, Tb-DBA shows high sensitivity, great selectivity, and low detection limit toward epinephrine (EP, the metabolic precursor of VMA). The bifunctional detector based on Tb-DBA inherently improves analytical reliability and greatly reduces the chance of false negatives/positives for NEURO diagnosis. In addition, a one-to-two logic gate based on the interaction between Tb-DBA and VMA was constructed for the analysis of VMA level, which can be further used for NEURO diagnosis. This work represents the first example to design a luminescent sensor coupled with multiple mechanisms in a single sensing platform for the diagnosis of NEURO, providing a new avenue for the clinical application of two-dimensional detection biomarkers for accurate diagnosis in serious diseases.

Introduction

Early diagnosis of cancer is a major societal concern due to its close association with clinical outcome and survival of patients. Therefore, the accurate detection of related biomolecules is crucial. Neuroblastoma (NEURO), a neuroendocrine tumor arising from adrenal medullary cells, is the most common tumor in children.[1–5] NEURO originates from primitive sympathetic ganglion cells and is characterized by excessive production of catecholamines (epinephrine EP) and their metabolites (vanillylmandelic acid VMA).[6–9] As a clinical indicator of NEURO, urinary VMA is produced in healthy individuals during a normal physiological process of $1.0–2.9 \times 10^{-5}$ M, whereas it is increased only threefold in the pathological process of NEURO.[10] Such minute changes in concentration are difficult to be distinguished precisely and can easily result

Shanghai Key Lab of Chemical Assessment and Sustainability, School of Chemical Science and Engineering, Tongji University, Siping Road 1239, Shanghai 200092, China. E-mail: byan@tongji.edu.cn

†Electronic supplementary information (ESI) available: The refinement details and additional figures. CCDC 2212905. For ESI and crystallographic data in CIF or other electronic format see DOI: https://doi.org/10.1039/d2qi02701a

in false positive/negative diagnostic results. Thus, exploring biosensors with ultrasensitive and robust responses to tiny changes in target concentrations is highly desirable for accurate diagnosis. In this respect, numerous methods, such as electrochemical,[11–13] gas chromatography-mass spectrometry (GC-MS),[14–16] high performance liquid chromatography coupled with electrochemical detection (HPLC-ECD)[17] and liquid chromatography-mass spectrometry (LC-MS)[18–20] have been developed to detect VMA levels. Nonetheless, these platforms still exist some intrinsic limitations: (1) Cumbersome sample preparation, long analysis time and susceptible to interference. (2) Most analytes require extensive and time-consuming derivatization to become stable, volatile and suitable for ionization techniques, resulting in poor utility. (3) Robust signal output conversion typically requires a target concentration greater than the intrinsic physiological range of the biological target. To overcome these limitations and improve the accuracy of biomolecules, we sought to design an optical biosensor with multiple response mechanisms and high sensitivity, which can provide ultrasensitive real-time determination of disease-related biomolecules within a small concentration window.

As a kind of the crystalline porous materials with structural tunability and functional versatility, luminescent metal–

1660 | *Inorg. Chem. Front.*, 2023, **10**, 1660–1670

This journal is © the Partner Organisations 2023

organic frameworks (MOFs)[21–28] have been considered as promising candidates for optical sensors. They not only offer the advantages of high sensitivity, fast response, simple operation and low cost as fluorescent sensors,[29–35] but can also be designed to perform Boolean logic operations[36–38] to transmit and process information, just like the human brain and electronics. Additionally, intelligent, decision-based molecular logic devices show great potential for life science applications.[39,40] These devices can handle binary and multi-valued information for multi-parameter chemical sensing,[41–45] disease diagnostics,[46–49] and biomedicine.[50–52] However, most previous MOF-based luminescent sensors are mainly based on a single monitoring mode or a single sensing mechanism, which is insufficient for reliable and accurate quantification of the target and prone to erroneous diagnostic results. Increasing the signal output and sensing channels would be beneficial to improve the reliability of detection. In 2019, Hao *et al.*, designed a luminescent sensor coupling multiple mechanisms in a single interface to determine DNA damage degree.[53] The fabricated single platform concurrently provided two switchable approaches for rapid quantitive and qualitative recognition of representative product of oxidative DNA damage by regulating the delicate competition between the different mechanisms. Given this, the construction of a practical logic device based on a multi-mechanism-driven luminescent sensor has the potential to create an optimized method for NEURO diagnostic monitoring. Herein, we report a novel strategy to design a dual-mechanism-driven Tb-MOF based biosensor (Tb-DBA) to track overexpressed VMA in urine by integrating the fluorescence resonant energy transfer (FRET) and

coordination effect into a single sensing platform. Excitation light can be well switched between the two mechanisms of expression and conversion by being rationally controlled. For VMA sensing, the sensor offers excellent performance with low limit of detection (LOD) (0.1 μM) and fast response (3 min). The sensor-based advanced analytical device can potentially respond to increasing VMA concentrations by dividing the output bits into three logical groups (YES (0, 0), OK (1, 0) and NO (1, 1)), which provides a simple analytical method for VMA detection relevant to NEURO diagnosis. It is worth noting that Tb-DBA can also occur with EP (a precursor of VMA) in an optical response not unlike that of VMA, adding reliability to the diagnosis of NEURO and largely avoiding false positive and negative results.

Experimental section

Synthesis and structural characterization of Tb-DBA

A hydrothermal reaction of $Tb(NO_3)_3 \cdot 6H_2O$ and H_2DBA in mixed solvents of *N,N*-dimethylformamide (DMF) and HNO_3 gave the yellow block crystal Tb-DBA. Single crystal X-ray diffraction study revealed that Tb-DBA crystallizes in a monoclinic space group $P2(1)/c$. The structure contains two Tb atoms, two DBA^{2-} ligands, one coordinated DMF molecule and one disordered DMF molecule per asymmetric unit. The Tb(1) is coordinated by seven oxygen atoms in triangular prism coordination geometry: one oxygen atom comes from a DMF, and the remaining six oxygen atoms come from the carboxylic acid groups of six different DBA^{2-} ligands (Fig. 1a). Two adjacent
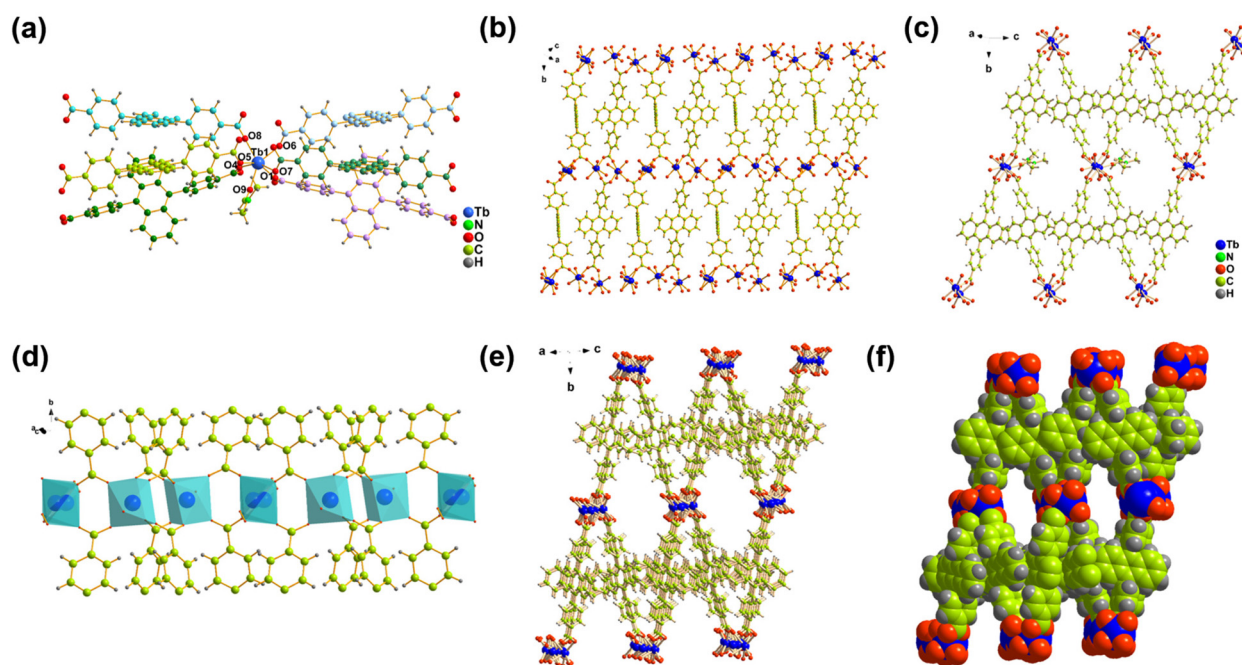

Fig. 1 (a) The coordination environment of the Tb(1) in Tb-DBA. (b) The 2D structure of the complex along the bc plane. (c) The inside of the 1D channel. (d) One dimensional chain structures formed by Tb(1) and Tb(2) motifs linked by DBA^{2-} linkers along a direction. (e) and (f) The 3D framework of Tb-DBA formed *via* 2D layers.

This journal is © the Partner Organisations 2023

Inorg. Chem. Front., 2023, **10**, 1660–1670 | **1661**

Tb(1) are interconnected by the carboxyl groups to produce a dimeric unit with a nonbonding Tb···Tb distance of 4.229 Å (Fig. S2†). The disordered Tb(2) is in a distorted octahedral coordination geometry, being coordinated by four oxygen atoms from four carboxylate groups of four different DBA^{2-} ligands, two oxygen atom from the carbonyl groups of two disordered DMF molecules respectively (Fig. S3†). A dimeric unit of Tb(1) and a Tb(2) are bridged by carboxyl groups of DBA^{2-} ligands to form a one-dimensional chain along the b direction (Fig. 1d). These chains were connected together by the deprotonated DBA^{2-} ligands to form a two-dimensional layered structure (Fig. 1b). Adjacent two-dimensional laminar structures are further interleaved by DBA^{2-} ligands to form a three-dimensional network structure (Fig. 1e and f). The three-dimensional framework exhibits open hexagonal channels filled with DMF molecules (Fig. 1c).

The synthesized Tb-DBA were characterized by scanning electron microscopy (SEM), powder X-ray diffraction (PXRD) and thermogravimetric analysis (TGA) to determine their purity and stability. As shown in Fig. 2a, the SEM image and elemental mapping showed that Tb-DBA had a blocky shape and the Tb element was uniformly distributed in the Tb-DBA. The diffraction peak of the Tb-DBA crystal sample was in good agreement with the simulation data of the single crystal structure, which confirmed the phase purity of the synthesized sample. As shown in Fig. S4,† the TGA analysis curve of Tb-DBA showed a weight loss of 11.35% between 130 and 360 °C, which corresponded to the loss of two DMF molecules (calculated 11.24%), and the structure was maintained until 440 °C. Additionally, the Fourier-transform infrared (FTIR) spectra of H$_2$DBA and Tb-DBA were recorded (Fig. S5†). There was a characteristic absorption peak at 1687 cm^{-1} in the spectra of

H$_2$DBA, which arose from C=O stretching vibrations of the free carboxyl group. Compared with the characteristic peaks of H$_2$DBA, in the FTIR spectra of Tb-MOF the stretching vibrations of C=O at 1671 cm^{-1} was red-shifted and the intensity of the peak was significantly decreased. Moreover, a new vibration band at 1147 cm^{-1} (belonging to the bending stretching of Tb-OH) appeared in the spectra of Tb-DBA, which suggested that Tb^{3+} ions are successfully coordinated with the H$_2$DBA ligands. Under the irradiation of 365 nm UV lamp, the luminescence color of Tb-DBA was obviously different from that of H$_2$DBA in the solid state. The corresponding CIE diagrams also showed the emission colors of the H$_2$DBA and Tb-DBA as dark blue (0.1418, 0.1175) and cyan (0.194, 0.2906), respectively (Fig. S6d†). Fig. S6a and b in the ESI† show the fluorescence spectra of the H$_2$DBA and Tb-DBA in the solid state at ambient temperature. The maximum emission wavelengths of H$_2$DBA and Tb-DBA under 396 nm excitation were 462 and 478 nm, which was almost in alignment with the characteristic emission peak of the ligand, indicating that the luminescence of Tb-DBA was emitted by the ligand rather than the central Tb^{3+} ions (Fig. S6c†). The first excited triplet energy level (T_1) of H$_2$DBA (16 496 cm^{-1}) is lower than the $^5D_4$ level of Tb^{3+} (20 500 cm^{-1}) by density functional theory calculation based on the b3lyp/6-31 g level, which explained why the complex did not show characteristic Tb^{3+} fluorescence. However, such luminescence characteristics provide the possibility for Tb-DBA to implement VMA sensing through a dual-mode strategy. To verify the feasibility of our synthesized Tb-DBA for VMA and EP detection, the stability of Tb-DBA in aqueous media was first tested, as VMA in urine and EP in serum were distributed in the aqueous phase. As shown in Fig. 2b and S7,† the crystal integrity and luminescence signal
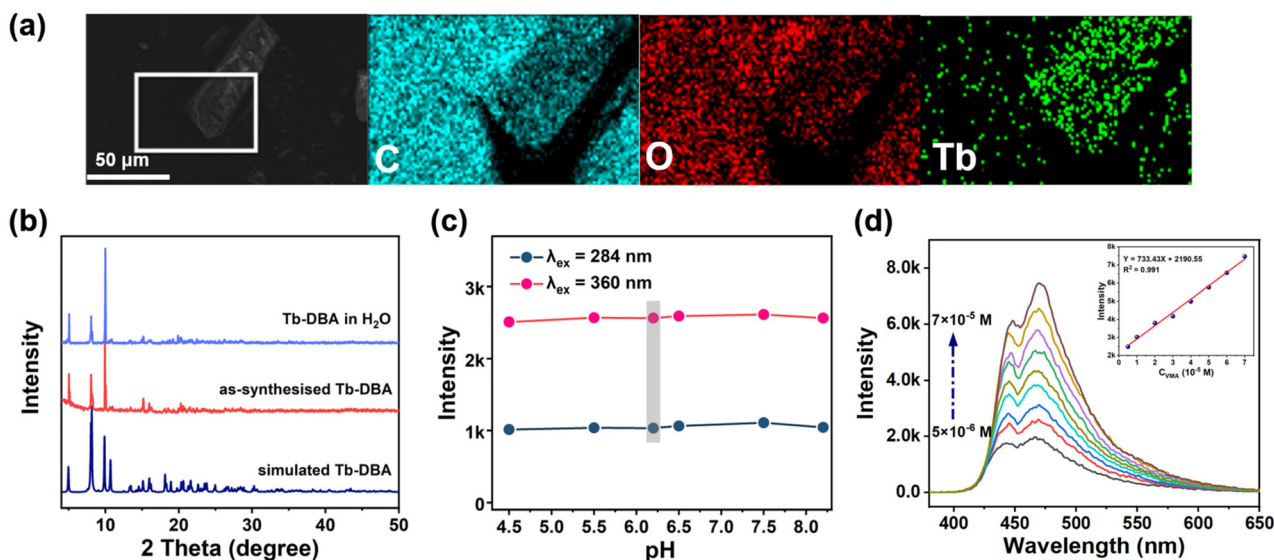
Fig. 2 (a) SEM and elemental mapping images of Tb-DBA. (b) PXRD patterns of simulated Tb-DBA (blue) and synthesised Tb-DBA before (red) and after (purple) storage in water for 24 h. (c) Effects of pH on the luminescence intensities of Tb-DBA at 468 nm. The points marked with gray bar represent the intensities of Tb-DBA in deionized water (pH = 6.2). (d) Luminescence spectra of Tb-DBA in the presence of 5 × 10^{-6}–7 × 10^{-5} M VMA aqueous solution (λ_{ex} = 360 nm). Inset: the corresponding calibration curves (λ_{em} = 468 nm).

1662 | *Inorg. Chem. Front.*, 2023, **10**, 1660–1670

This journal is © the Partner Organisations 2023

of Tb-DBA did not change significantly after immersion in aqueous solution after 24 h, indicating that Tb-DBA has good chemical and optical stability in aqueous environment. In addition, the pH-dependent luminescence and structural properties in the urine and serum pH range (4.5–8.2) were also investigated (Fig. 2c and S8†). Tb-DBA showed negligible fluorescence changes in this pH range without any loss of crystallinity, indicating the feasibility of Tb-DBA as sensing materials in aqueous media at biological urine and serum environments. This exceptional water stability is attributed to the hydrophobicity of the anthracene-based organic ligand and the strong Tb–O coordination bond, which makes the framework resistant to attack and hydrolysis by water molecules.[54]

Dual switchable detection performances of Tb-DBA with VMA

Then, the luminescence behaviors of Tb-DBA suspensions in the presence of VMA were measured. Upon adding VMA to the Tb-DBA suspension, the Tb-DBA's maximum emission peak at 468 nm increased to 3.8 times under excitation at 360 nm (Fig. 2d). Interestingly, the excitation spectrum of Tb-DBA-VMA showed a new peak at 264 nm compared to the original Tb-DBA excitation spectrum (Fig. S9a†). The emission pattern of Tb-DBA-VMA also changed under the excitation of 264 nm. The dual emission of Tb-DBA-VMA can be observed in Fig. S9b,† one based on the ligand emission at 433 nm and the other with four characteristic peaks of Tb^{3+} ions at 487, 544, 584 and 621 nm. By monitoring the 544 nm emission peak, the best excitation wavelength of Tb-DBA-VMA was exhibited at 286 nm (Fig. S9c†). As shown in Fig. S9d,† the characteristic emission of Tb^{3+} was significantly enhanced, while the emission at 468 nm kept stable under the excitation at 286 nm. When the original fluorescence intensity ratio at 544 and 468 nm ($I_{544}/I_{468} = 0.22$) is defined as 1.0, the relative fluorescence intensity ratio increased by 14.2 times after the addition of VMA. Two completely different fluorescence responses of Tb-DBA to VMA were observed as the excitation wavelength was switched from 360 nm to 286 nm, which enabled the Tb-DBA to be a light-regulated optical sensor for VMA with two tunable recognition patterns. The switchable luminescence responses modulated by different excitation lights are ascribed to a competitive effect of the fluorescence resonant energy transfer (FRET) between VMA and the ligand in Tb-DBA and the energy transfer (ET) induced by ligand-to-metal charge transfer (LMCT) between VMA with the Tb^{3+}, which was confirmed by PXRD, lifetime measurements, UV-Vis, FT-IR spectra, *etc*. The PXRD pattern did not change after the experiment of Tb-DBA with VMA, indicating that the framework of Tb-DBA did not collapsed in VMA solution (Fig. S10†). In addition, the luminescence lifetime of Tb-DBA at 468 nm increased from 7.423 to 11.848 ns in the time-resolved fluorescence decay spectrum under excitation of 360 nm after the VMA treatment (Fig. S11 and Table S2†), which suggested an interaction between Tb-DBA and VMA. As shown in Fig. S12,† the excitation peak of Tb-DBA at 340–398 nm is well overlapped with the emission peak of VMA at 397 nm, illustrating a great energy level match between the

singlet excited states (S_1 level) of donor (VMA) and acceptor (Tb-DBA). The great energy level match effectively promotes the FRET process from the S_1 level of D–A dual-component VMA (4.9538 eV) to S_1 level of ligand in Tb-DBA (3.1154 eV). In addition, the LUMO level of VMA (−0.33 eV) is obviously higher than that of ligand in Tb-DBA (−1.91 eV), indicating the excited electrons of VMA in its LUMO can transfer to the LUMO of Tb-DBA and the PET process contributes to the luminescence enhancement. Therefore, the PET from VMA to H_2DBA molecule in Tb-DBA can be responsible for the FRET between VMA and Tb-DBA, which was the dominant driving force to the turn-on luminescence behavior under excitation of 360 nm. In contrast to the lifetime change behavior of 360 nm excitation, the lifetime of [Tb-DBA-VMA] adduct at 468 nm (Fig. S13†) exhibited a very slight change under 286 nm excitation. At $\lambda_{ex} = 286$ nm, [Tb-DBA-VMA] adduct generates four obvious emission peaks at 487, 544, 584 and 621 nm originating from $^5D_4 \rightarrow {^7F_K}$ ($K = 3, 4, 5, 6$) transitions of Tb^{3+} ions and ligand-based emission at 468 nm. The decay lifetime of the 544 nm emission peak for [Tb-DBA-VMA] adduct follows the exponential equation [$I = A_1\exp(-t/\tau_1) + I_0$], and the lifetime is 399.84 μs (Fig. S14†). The photoluminescence performance of [Tb-DBA-VMA] adduct reveals that the ET induced by LMCT from VMA to Tb^{3+} ions allows Tb-DBA to generate green emission. Moreover, the relative fluorescence response of VMA toward Tb^{3+} was also investigated. It was found that free VMA molecules display an intense emission band at 410 nm upon excitation at 306 nm, which may be caused by the π*–π transition (Fig. S9e†). Interestingly, complex VMA-Tb^{3+} exhibits the emission peaks at 489, 544, 585 and 620 nm originating from Tb^{3+} besides the emission at 377 nm based on VMA when excited at 310 nm. By monitoring the 545 nm emission peak, the best excitation wavelength of VMA-Tb^{3+} was exhibited at 294 nm (Fig. S9f†). Compared to the free VMA, complex (VMA-Tb^{3+}) not only exhibits the characteristic emission of Tb^{3+}, but also the ligand-based emission is blue-shifted by 33 nm, suggesting that the LMCT-induced ET based on VMA procedure effectively promotes the emission of Tb^{3+} in Tb-DBA. After adding Tb-DBA into the VMA solution, the solution was centrifugated and the supernatant was collected for recording UV adsorption spectra. From the UV absorption spectrum shown in Fig. 3d, we can see that the UV absorption intensity of VMA with the addition of Tb-DBA was significantly lower compared to the original VMA, indicating the enrichment effect of Tb-DBA on VMA through the coordination between Tb^{3+} and VMA. After that, the FTIR spectra of Tb-DBA and Tb-DBA-VMA have been recorded and analyzed. As shown in Fig. 3a, the peaks at 1240 and 1031 cm^{-1} for free VMA are considered to be characteristic C–O stretching vibrational peaks for aromatic ethers and are shown at 1239 and 1035 cm^{-1} for VMA-impregnated Tb-DBA. It was also found that the characteristic peaks of 1745 and 1147 cm^{-1} for VMA belonging to the stretching vibration of the C=O bond and C-OH (–COOH group) shift to 1682 and 1130 cm^{-1} for Tb-DBA-VMA, which further demonstrated the coordinated chelation of carboxyl groups in the VMA and Tb^{3+} in Tb-DBA.
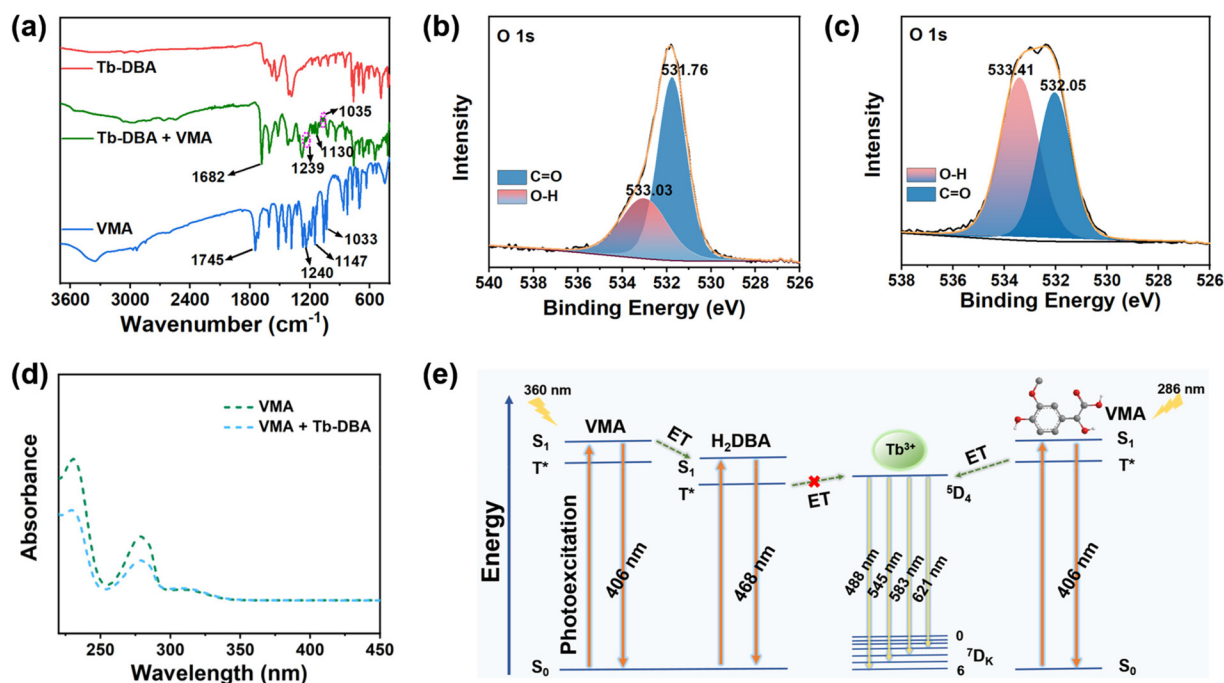
Fig. 3 (a) FT-IR spectra of VMA (blue), Tb-DBA (red) and after treatment with VMA (green). (b) XPS spectra of O 1s electrons in Tb-DBA and (c) in Tb-DBA+VMA. (d) UV-Vis spectra of the VMA and after treatment with Tb-DBA. (e) Schematic of the dominant mechanism in the excitation light-operated luminescence.

Furthermore, the ^{1}H NMR analysis of the Tb-DBA solid after immersion in aqueous solution containing VMA also demonstrated that VMA could be coordinated to Tb^{3+} by replacing the DMF molecules in the channel of Tb-DBA (Fig. S15†). Additionally, the interaction between VMA and Tb^{3+} of Tb-DBA was also verified by X-ray photoelectron spectroscopy (XPS) of Tb and O elements. Two XPS peaks at 1277.3 and 1243.7 eV of Tb 3d in Tb-MOF (Fig. S16†) were shifted from 1277.1 eV to 1242.9 eV, suggesting that Tb^{3+} attracted the electrons in carboxyl oxygen of VMA after coordinating with Tb^{3+}, increasing the electron cloud density of Tb atom and reducing the binding energy. In the O 1s spectra (Fig. 3b and c), Tb-DBA presents two O 1s XPS peaks at 533.03 eV (O—H bond) and 531.76 eV (C=O bond) and the intensity ratio of C=O and O—H bonds was 1 : 0.53. By contrast, the two O 1s peaks of Tb-DBA-VMA were located respectively at 533.41 eV (O–H bond) and 532.05 eV (C=O bond) and the intensity ratio of C=O and O–H bonds was 1 : 0.88. The increase of the O–H bond intensity further suggests that the VMA molecules with multiple hydroxyl groups was coordinated with Tb^{3+} in Tb-DBA. Furthermore, the first excited triplet energy of VMA was at 21 160 cm^{-1}, calculated using density functional theory based on the b3lyp/6-31 g level, which is close to the $^5D_4$ energy level of the rare-earth ion Tb^{3+}. It was proved that the effective transformation of energy from VMA to Tb^{3+} could be realized in theory. These experimental results suggested that Tb-DBA could be used as a light-operated dual-mechanism-driven platform for the detection of VMA through the competitive effect

of the FRET between VMA and the ligand in Tb-DBA and the ET induced by LMCT between VMA with the Tb^{3+} (Fig. 3e).

For fluorescence sensing, sensing sensitivity, interference immunity, detection limit and response time are a series of important parameters. Considering the VMA range for healthy (1.0–2.9 × 10^{-5} M) and diseased (3.0–9.5 × 10^{-5} M), the linear range of Tb-DBA quantification was limited to the biologically relevant concentration window (10^{-5}–10^{-4} M). After exposing Tb-DBA to a VMA solution with a series of concentrations (5 × 10^{-6} to 7 × 10^{-5} M) for 1 min, the luminescence spectra of Tb-DBA were recorded respectively under 360 and 286 nm excitation. When the material was excited at 360 nm, the intensity of the emission at 468 nm was continuously enhanced, and there was a linear relationship between the values of I_{468} and C with a correlation coefficient (R^2) of 0.991 (inset of Fig. 2d). When excited at 286 nm, the emission peak at 468 nm had no change basically, but the intensity of green emissions at 487, 544, 584 and 621 nm increased successively with the growing concentration of VMA (Fig. 4a), which resulted in an apparent emission color changes from blue (0.1754, 0.1669) to cyan (0.2381, 0.3589) in the relative CIE diagram (Fig. 4d). As seen in Fig. S9d,† the excitation spectrum of Tb-DBA with VMA was monitored at 286 nm when the optimal emission was 544 nm, which is not in the optimal excitation range of 295–410 nm based on the emission at 468 nm. This result illustrates the phenomenon that the emission intensity of Tb-DBA at 468 nm remained almost constant with the titration of VMA. The ratio of emission peaks at 544 and 468 nm can be determined to
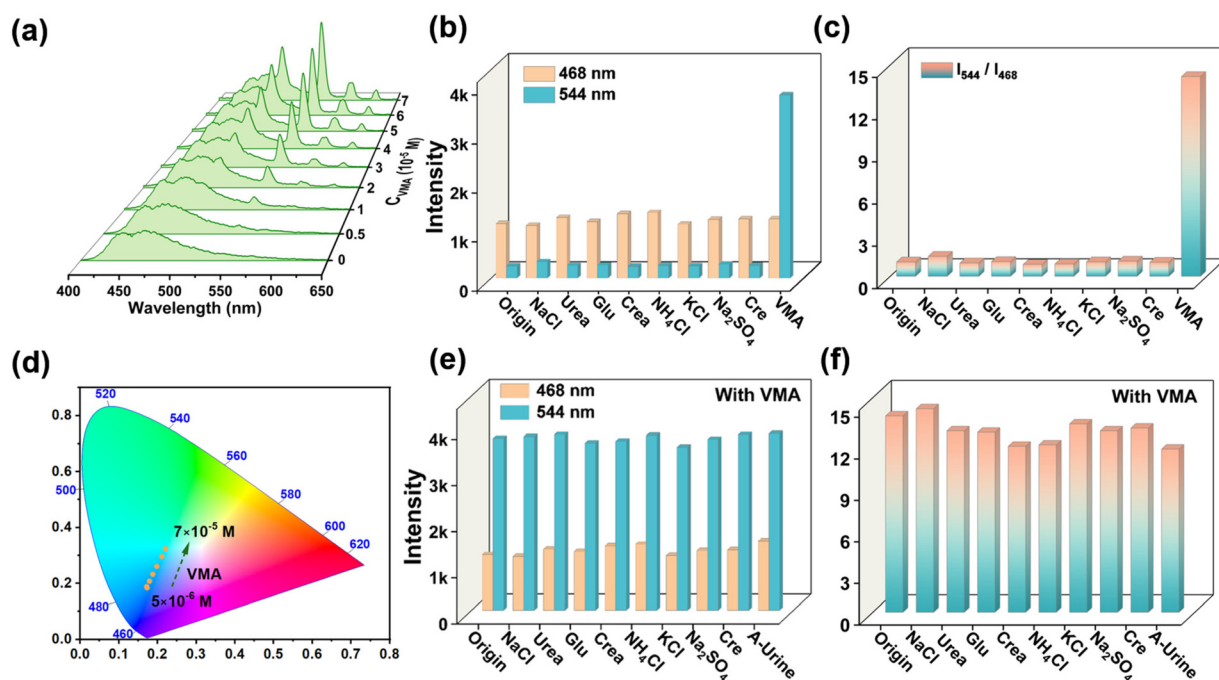
1664 | *Inorg. Chem. Front.*, 2023, **10**, 1660–1670

This journal is © the Partner Organisations 2023

Fig. 4 (a) Luminescence spectra of Tb-DBA in aqueous solution of VMA at various concentrations ($C = 5 \times 10^{-6}$ to 7×10^{-5} M and $\lambda_{ex} = 286$ nm). (b) and (c) Emission intensity of Tb-DBA induced by VMA and various biologically coexisting species at 468 nm, 544 nm and its ratio variation under excitation at 286 nm. (d) CIE chromaticity coordinates of Tb-DBA in the presence of VMA at different concentrations under the excitation of 286 nm. (e) and (f) The luminescence intensity response of Tb-DBA to VMA at 468 nm and 544 nm and its ratio in the background of various other urine components ($\lambda_{ex} = 286$ nm).

realize the quantitative detection of VMA with a great linear correlation ($I_{544}/I_{468} = 0.559 C_{VMA} - 0.383$, $R^2 = 0.986$) in the concentration range of 10^{-5} to 6×10^{-5} M (Fig. S17†), which indicates that the chromatic and ratiometric sensing of Tb-DBA toward VMA was achieved under 286 nm excitation. These results imply that Tb-DBA can be used as an excellent luminescence sensor for the quantitative analysis of VMA in aqueous solutions over the biologically relevant concentration window regardless of the excitation wavelength. The limits of detection (LODs) were 1.08 and 1.22×10^{-7} M at 360 and 286 nm excitation, respectively, according to $3\sigma/k$ (σ is the standard deviation of the fluorescence measurement of 20 replicates of the blank solution and k is the slope of the obtained linear curve). Both LODs are well below the normal human threshold (3×10^{-5} M) and are suited for negative or positive expression in the diagnosis of NEURO. It is worth emphasizing that this fluorescence sensing strategy gives two quantitative detection pathways for VMA in one platform simultaneously. The integration of both approaches into a single sensing platform avoids erroneous results and improves the reliability of its quantitative detection compared to single mechanism/modality-driven sensors. In order to investigate the specificity of Tb-DBA for VMA detection, we investigated the luminescence of Tb-DBA in different simulated urine species since VMA is metabolized in urine. As shown in Fig. 4b and c and Fig. S18a in the ESI,† under excitation at 286 and 360 nm, the addition of other typical urine species (NaCl, urea, glucose,

creatinine, NH$_4$Cl, KCl, creatine and Na$_2$SO$_4$) resulted in only negligible intensity changes, much lower than the values for the addition of VMA. Encouraged by this result, the anti-interference ability of the sensor was further evaluated by fluorescence intensity detection in aqueous suspension of Tb-DBA with VMA in the presence of various interferents simulating urine. When the excitation wavelengths were 286 and 360 nm, the proposed biosensor exhibited excellent performance for VMA discrimination in both mixed analytes and artificial urine. Fig. 4e and f showed that the apparent changes in emission intensity and ratio triggered by VMA at 468 and 544 nm were almost independent of the various coexisting species and artificial urine background. After that, we examined the feasibility of this method in biological matrices by analyzing artificial urine samples spiked with different concentrations of VMA using Tb-DBA at two different excitation wavelengths. In Fig. S19a and S20a,† artificial urine was used instead of aqueous solution to prepare the VMA stock solution, and their effects on the optical signal of Tb-DBA under 360 and 286 nm excitation were recorded with increasing VMA concentration, respectively. The similar fluorescence responses of the probes in synthetic urine samples and aqueous samples at VMA concentrations of $1–13 \times 10^{-5}$ M further demonstrate that Tb-DBA can monitor VMA in artificial urine in dual mode, independent of complex biological systems. The linearity of the emission intensity of Tb-DBA at 468 nm under 360 nm excitation *versus* the concentration of VMA with a correlation coefficient

This journal is © the Partner Organisations 2023

Inorg. Chem. Front., 2023, **10**, 1660–1670 | **1665**

(R^2) of 0.985 and a calculated LOD of 2.1×10^{-7} M (Fig. S19b†). At λ_{ex} = 286 nm, the ratio of emission peaks at 544 and 468 nm can be determined to realize the quantitative detection of VMA in synthetic urine with a LOD of 2.5×10^{-7} M (Fig. S20b†). These results demonstrate the excellent selectivity and anti-interference ability of the dual mechanism-driven Tb-DBA for VMA in various urine components and artificial urine.

Fluorescence response and sensing mechanism of Tb-DBA to EP

NEURO is a rare neuroendocrine tumor arising from adrenal medullary cells and is characterized by excessive production of EP and its metabolites (VMA). Since the EP level in serum is closely related to NEURO, the simultaneous detection of EP in serum and VMA in urine based on a sensing platform will undoubtedly improve the reliability of the diagnosis of NEURO. The luminescence spectra of Tb-DBA were recorded after adding ground Tb-DBA powder into an aqueous solution of EP (17×10^{-6} M) for 30 s, and the fluorescence enhancement was found to be up to 6.7 times. Under 360 nm excitation, the intensity of the emission peak based on 468 nm gradually increased with increasing VMA concentration and slightly blue-shifted toward 435 nm, resulting in the obvious blue luminescence of Tb-DBA (Fig. 5a). There was a good linear relationship (R^2 = 0.994) between the response signals and the EP concentration in the range of $1–17 \times 10^{-6}$ M, with a calculated LOD of 2.8×10^{-8} M (Fig. 5b). The Tb-DBA emission color changes from blue (0.1754, 0.1669) to dark blue (0.1591, 0.0841) with increasing EP concentration in the relative CIE diagram (Fig. 5c), which in sharp contrast with the phenomenon of adding VMA at 286 nm excitation. In addition, different serum components (KCl, glucose, NaCl, L-proline, MgCl$_2$, urea, NaHCO$_3$, and CaCl$_2$) were investigated in order to

verify the detection selectivity of Tb-DBA for the EP. As shown in Fig. S21,† the luminescence of Tb-DBA remained essentially unchanged with the addition of other components in serum, except for the same concentration of EP, indicating that Tb-DBA can be used as a sensor for EP with high sensitivity and selectivity, and offering the possibility to detect it in real serum samples. Subsequently, the recorded optical signals are shown in Fig. S22a,† the luminescence response of Tb-DBA in goat serum was similar to that of the aqueous solution, demonstrating that Tb-DBA can detect EP in serum without interference from other biological components. Fig. S22b† shows the calibration curve for the EP detection in the range of $2–20 \times 10^{-6}$ M with a linear correlation coefficient R^2 of 0.988 and an LOD of 2.2×10^{-8} M, which implies that the Tb-DBA is an excellent fluorescence sensor for the quantitative monitoring of EP. The consistent PXRD patterns of Tb-DBA samples before and after EP treatment not only confirmed the structural stability of Tb-DBA (Fig. S10†), but also automatically excluded the fluorescence enhancement based on structural collapse. In the time-resolved fluorescence decay spectra, the luminescence lifetime of Tb-DBA at 435 nm increased from 8.022 ns to 16.389 ns after EP treatment (Fig. S23†), indicating an interaction between Tb-DBA and EP. To confirm whether the mechanism of fluorescence enhancement was caused by PET, the LUMO and HOMO energy values of EP molecules and H$_2$DBA were estimated and compared by density flooding theory calculations. As illustrated in Fig. 5d, both LUMO and HOMO energy values of H$_2$DBA were lower than those of EP, which could facilitate the PET process from EP to the ligand in Tb-DBA. Furthermore, the S$_1$ level of EP (4.9761 eV) was higher than that of H$_2$DBA (3.1154 eV), which was responsible for the PET-based energy transfer process from the EP unit to Tb-DBA. All these results suggest that Tb-DBA can be used as a bifunctional detector for sensing EP and VMA through different fluorescence response phenomena to improve the reliability and accuracy of NEURO diagnosis.
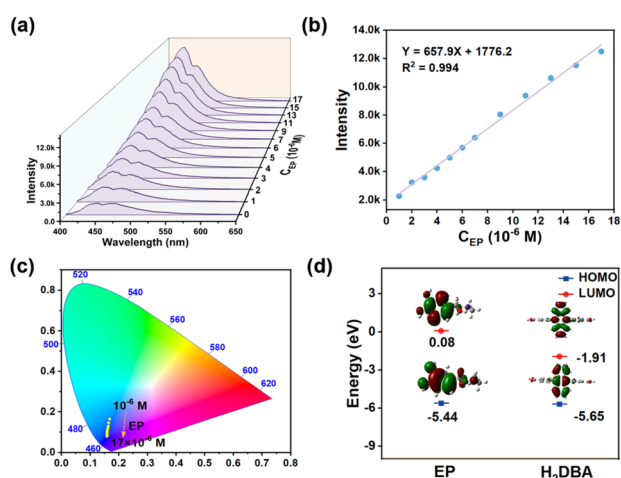
Construction of logic gates

Logic gates are functional devices for information processing that show great potential in many life science applications such as disease diagnosis, biomarker detection, data storage, and prodrug activation. Current research on logic gates has focused on basic logic functions, AND, NOR, OR, IMP, INH, and XOR, while building complex molecular devices with multiple inputs remains challenging. When more inputs are integrated, the complexity of logic operations increases and general and more powerful functions can be implemented by connecting different logic gates. Herein, a cascaded logic gate consisting of an INHIBIT gate and an AND gate was designed based on the interaction between the excitation wavelength and the VMA (Fig. 6a). In the operation of this combined gate, λ_{360} (excitation at 360 nm), VMA and λ_{286} (excitation at 286 nm) were selected as input 1, input 2 and input 3, respectively, and the emission intensity at 544 nm (F_{544}) was used as the output. The emission at 544 nm based on Tb-DBA-VMA cannot appear at λ_{360}, so the λ_{360} and VMA were designed as

Fig. 5 (a) Emission spectra (λ_{ex} = 360 nm) of Tb-DBA immersed in various concentrations of EP ($1–17 \times 10^{-6}$ M). (b)The dependence of the emission intensity of Tb-DBA on the concentration of EP. (c) CIE chromaticity coordinates of Tb-DBA in the presence of EP at different concentrations under the excitation of 360 nm. (d) The LUMO and HOMO orbitals of EP and H$_2$DBA.

1666 | *Inorg. Chem. Front.*, 2023, **10**, 1660–1670

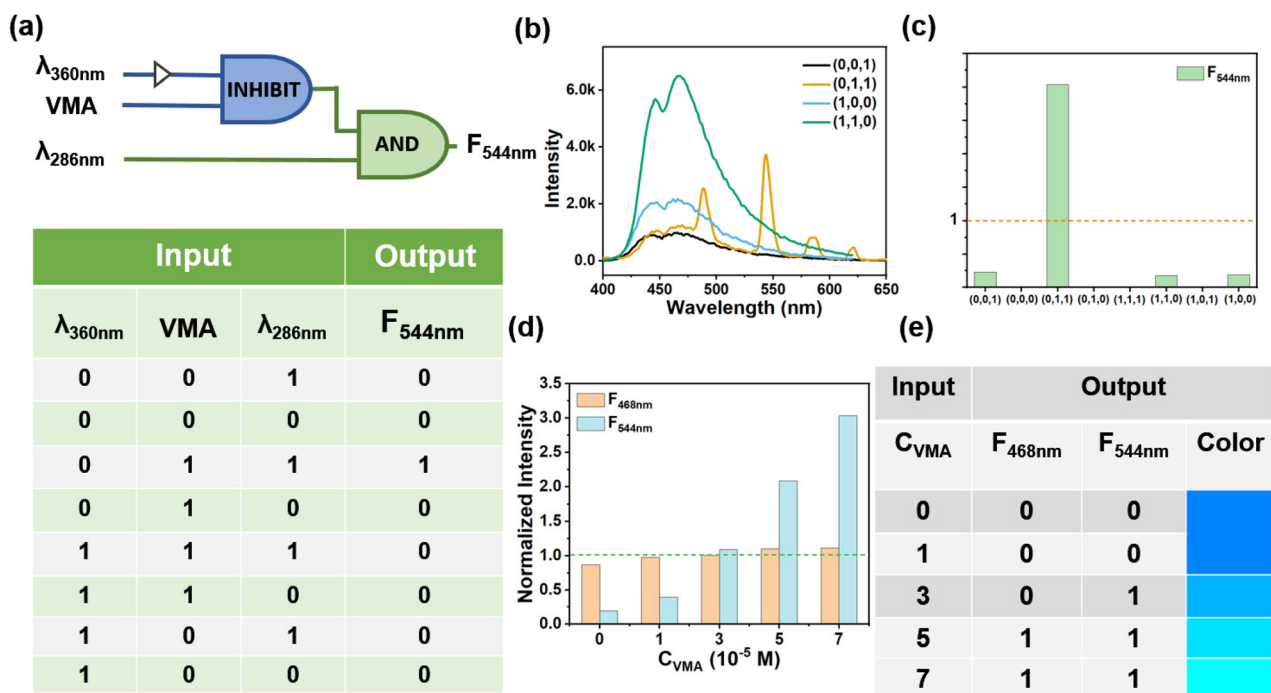This journal is © the Partner Organisations 2023

Fig. 6 (a) Scheme and electronic equivalent circuitry of the cascaded logic gate (INHIBIT+AND) and the truth table of the cascaded logic gate (b) PL spectra of the cascaded logic gate. (c) Column diagram of the emission peaks at 544 nm: the dashed line shows the threshold. (d) Column diagram of the normalized fluorescence intensity of emission peaks at 544 and 468 nm toward different concentration of VMA ranging from 0 to 7 × 10^{-5} M. (d) Truth table of the one-to-two logic analytical device for VMA monitoring.

two inputs to construct the INHIBIT gate. The 544 nm-based emission occurred only when VMA and λ_{286} were introduced simultaneously, since the excitation wavelength at 286 nm is the optimal emission of Tb^{3+} in Tb-DBA-VMA, and thus the λ_{286} and VMA were used as two inputs to construct the AND gate (Fig. 6b). The presence and absence of the three inputs were denoted as "1" and "0", respectively, with a threshold value of 1 (the maximum concentration of VMA in healthy human urine makes the corresponding normalized fluorescence intensity at 544 nm) (Fig. 6c). From the truth table in Fig. 6a, it is clear that the output is "1" only when the inputs are (0,1,1), and "0" when the inputs are otherwise. In addition, the simplest one-to-two decoder that converts one input into two outputs is designed to detect the VMA concentration level based on the interaction between Tb-DBA and VMA. For the input, the presence and absence of VMA are defined as "1" and "0", respectively, and the normalized fluorescence signals of F_{468} (emission intensity at 468 nm) and F_{544} are used as dual outputs with a threshold value of 1. Fig. S24† gives the normalized fluorescence intensity histograms of the logic gates of the one-to-two decoder and the corresponding truth tables and show the different responses of the Tb-DBA for various input states. By dividing the output area into three logical groups, the one-to-two decoder logic gate can be designed as a more advanced analysis device that can respond to increasing VMA concentrations: YES (0, 0), OK (1, 0), and NO (1, 1). Here, five concentrations from 0 to 7 × 10^{-5} M were

set as input signals and the output signals were normalized (Fig. 6d). As shown in Fig. 6e, the OK gate was triggered by 3 × 10^{-5} M VMA and the NO gate was triggered by 6 × 10^{-5} M VMA. The YES gate appears when the concentration was below 3 × 10^{-5} M. Therefore, the VMA concentration level can be generated as a simple binary code to output a (1, 1) code representing a high concentration of VMA. Any other codes (0, 0 and 0, 1) reflect that the VMA concentration is within the human health concentration range. Each concentration can correspond to a color which can be observed from CIE (Fig. 4d) by using the emission spectra calculated in Fig. 4a. Then the concentrations (0 to 7 × 10^{-5} M) were divided into four ranges with representative colors as shown in Fig. 6e, 0–1 (dark blue), 1–3 (light blue), 3–5 (cyan) and 5–7 (green), and the designed the logic device can perform well in analyzing the VMA levels by color discrimination.

Conclusions

In summary, we designed and synthesized Tb-MOF (Tb-DBA) with high water and thermal stability as a biosensor for the simultaneous detection of VMA and its metabolic precursor EP, both of which are key indicators for the clinical diagnosis of neuroblastoma. The designed light-controlled dual-mode driven platform (Tb-DBA) was able to provide two simultaneous VMA assays with rapid and ultra-sensitive detection

This journal is © the Partner Organisations 2023

Inorg. Chem. Front., 2023, **10**, 1660–1670 | **1667**

capabilities by the competitive action of FRET between VMA and ligands in Tb-DBA and LMCT-induced ET between VMA and Tb^{3+}, reducing the chance of erroneous results from these single-method driven assay platforms. More importantly, Tb-DBA, as a luminescent probe, can quantitatively identify VMA in urine in a dual mode of chromaticity and ratio under 286 nm excitation, thus significantly improving the diagnostic accuracy of neuroblastoma. In addition, an advanced analytical device based on a cascaded logic gate and a one-to-two decoder was established and successfully combined with the fluorescence sensing of VMA, which performed well in analyzing VMA levels for neuroblastoma diagnosis. This work is the first example of a MOF-based luminescent probe for the simultaneous detection of biometabolites and their precursors, and propose a simple and novel strategy to modulate the optical response performance of multimodal analysis, opening new avenues for a versatile analytical platform for disease diagnosis.

Author contributions

B. Y. designed the experiment and revised the manuscript. Y. L. prepared the materials, measured the photoluminescence properties, collected pictures and wrote the manuscript.

Conflicts of interest

The authors declare that they have no competing interests.

Acknowledgements

References

1 E. Almstedt, R. Elgendy, N. Hekmati, E. Rosen, C. Warn, T. K. Olsen, C. Dyberg, M. Doroszko, I. Larsson, A. Sundstrom, M. Arsenian Henriksson, S. Pahlman, D. Bexell, M. Vanlandewijck, P. Kogner, R. Jornsten, C. Krona and S. Nelander, Integrative discovery of treatments for high-risk neuroblastoma, *Nat. Commun.*, 2020, **11**, 71.

2 B. M. Verhoeven, S. Mei, T. K. Olsen, K. Gustafsson, A. Valind, A. Lindstrom, D. Gisselsson, S. S. Fard, C. Hagerling, P. V. Kharchenko, P. Kogner, J. I. Johnsen and N. Baryawno, The immune cell atlas of human neuroblastoma, *Cell Rep. Med.*, 2022, **3**, 100657.

3 L. Jubierre, C. Jimenez, E. Rovira, A. Soriano, C. Sabado, L. Gros, A. Llort, R. Hladun, J. Roma, J. S. Toledo, S. Gallego and M. F. Segura, Targeting of epigenetic regulators in neuroblastoma, *Exp. Mol. Med.*, 2018, **50**, 1–12.

4 K. K. Matthay, J. M. Maris, G. Schleiermacher, A. Nakagawara, C. L. Mackall, L. Diller and W. A. Weiss, Neuroblastoma, *Nat. Rev. Dis. Primers*, 2016, **2**, 16078.

5 E. R. Pastor and S. A. Mousa, Current management of neuroblastoma and future direction, *Crit. Rev. Oncol. Hematol.*, 2019, **138**, 38–43.

6 L. L. Stafman and E. A. Beierle, Cell Proliferation in Neuroblastoma, *Cancers*, 2016, **8**, 13.

7 B. Qiu and K. K. Matthay, Advancing therapy for neuroblastoma, *Nat. Rev. Clin. Oncol.*, 2022, **19**, 515–533.

8 A. P. Berbegall, D. Bogen, U. Potschger, K. Beiske, N. Bown, V. Combaret, R. Defferrari, M. Jeison, K. Mazzocco, L. Varesio, A. Vicha, S. Ash, V. Castel, C. Coze, R. Ladenstein, C. Owens, V. Papadakis, E. Ruud, G. Amann, A. R. Sementa, S. Navarro, P. F. Ambros, R. Noguera and I. M. Ambros, Heterogeneous MYCN amplification in neuroblastoma: a SIOP Europe Neuroblastoma Study, *Br. J. Cancer*, 2018, **118**, 1502–1512.

9 I. S. Fetahu and S. Taschner-Mandl, Neuroblastoma and the epigenome, *Cancer Metastasis Rev.*, 2021, **40**, 173–189.

10 A. Němečková-Makrlíková, F.-M. Matysik, T. Navrátil, J. Barek and V. Vyskočil, Determination of three Tumor Biomarkers (Homovanillic Acid, Vanillylmandelic Acid, and 5-Hydroxyindole-3-Acetic Acid) Using Flow Injection Analysis with Amperometric Detection, *Electroanalysis*, 2019, **31**, 303–308.

11 B. Fu, H. Chen, Z. Yan, Z. Zhang, J. Chen, T. Liu and K. Li, A simple ultrasensitive electrochemical sensor for simultaneous determination of homovanillic acid and vanillylmandelic acid in human urine based on MWCNTs-Pt nanoparticles as peroxidase mimics, *J. Electroanal. Chem.*, 2020, **866**, 114165.

12 A. L. Squissato, R. A. A. Munoz, C. E. Banks and E. M. Richter, An Overview of Recent Electroanalytical Applications Utilizing Screen–Printed Electrodes Within Flow Systems, *ChemElectroChem*, 2020, **7**, 2211–2221.

13 F. Moncer, N. Adhoum, D. Catak and L. Monser, Electrochemical sensor based on MIP for highly sensitive detection of 5-hydroxyindole-3-acetic acid carcinoid cancer biomarker in human biological fluids, *Anal. Chim. Acta*, 2021, **1181**, 338925.

14 Y. Shen, J. Lu, Q. Tang, Q. Guan, Z. Sun, H. Li and L. Cheng, Rapid, easy analysis of urinary vanillylmandelic acid for diagnostic testing of pheochromocytoma by liquid chromatography tandem mass spectrometry, *J. Chromatogr. B Biomed. Appl.*, 2015, **1002**, 92–97.

15 M. K. Kolentinis, I. I. Verginadis, Y. V. Simos, N. C. Tsitou, S. C. Karkabounas, T. M. Kolettis and A. M. Evangelou, Cardiovascular effects of vanillylmandelic acid in rats, *Eur. J. Pharmacol.*, 2013, **703**, 46–52.

16 Y. Shen, H. Li, J. Lu, X. Luo, Q. Guan and L. Cheng, Analytical validation and clinical application of urinary vanillylmandelic acid and homovanillic acid by LC-MS/MS

1668 | *Inorg. Chem. Front.*, 2023, **10**, 1660–1670

This journal is © the Partner Organisations 2023

for diagnosis of neuroblastoma, *Biomed. Chromatogr.*, 2019, **33**, 4484.

17 T.-T. Du, T. Cui, H.-M. Qiu, N.-R. Wang, D. Huang and X.-H. Jiang, Simultaneous determination of tryptophan, kynurenine, kynurenic acid and two monoamines in rat plasma by HPLC-ECD/DAD, *J. Pharm. Biomed. Anal.*, 2018, **158**, 8–14.

18 Z. D. Clark, J. M. Cutler, I. Y. Pavlov, F. G. Strathmann and E. L. Frank, Simple dilute-and-shoot method for urinary vanillylmandelic acid and homovanillic acid by liquid chromatography tandem mass spectrometry, *Clin. Chim. Acta*, 2017, **468**, 201–208.

19 A. J. Pandopulos, C. Gerber, B. J. Tscharke, J. O'Brien, J. M. White and R. Bade, A sensitive analytical method for the measurement of neurotransmitter metabolites as potential population biomarkers in wastewater, *J. Chromatogr. A*, 2020, **1612**, 460623.

20 C. L. Sweeney, J. L. Bennett, C. A. M. Brown, N. W. Ross and G. A. Gagnon, Validation of a QuEChERS method for extraction of estrogens from a complex water matrix and quantitation via high-performance liquid chromatography-mass spectrometry, *Chemosphere*, 2021, **263**, 128315.

21 G.-L. Yang, X.-L. Jiang, H. Xu and B. Zhao, Applications of MOFs as Luminescent Sensors for Environmental Pollutants, *Small*, 2021, **17**, 2005327.

22 K. Zhou, C. Zhang, Z. Xiong, H.-Y. Chen, T. Li, G. Ding, B. Yang, Q. Liao, Y. Zhou and S.-T. Han, Template–Directed Growth of Hierarchical MOF Hybrid Arrays for Tactile Sensor, *Adv. Funct. Mater.*, 2020, **30**, 2001296.

23 M. Daniel, G. Mathew, M. Anpo and B. Neppolian, MOF based electrochemical sensors for the detection of physiologically relevant biomolecules: An overview, *Coord. Chem. Rev.*, 2022, **468**, 214627.

24 P. Iacomi, E. Gulcay-Ozcan, P. Pires Conti, S. Biswas, N. Steunou, G. Maurin, G. Rioland and S. Devautour-Vinot, MIL-101(Cr) MOF as an Effective Siloxane Sensor, *ACS Appl. Mater. Interfaces*, 2022, **14**, 17531–17538.

25 Y. Cao, L. Wang, C. Shen, C. Wang, X. Hu and G. Wang, An electrochemical sensor on the hierarchically porous Cu-BTC MOF platform for glyphosate determination, *Sens. Actuators, B*, 2019, **283**, 487–494.

26 Q. Xia, W. Li, X. Zou, S. Zheng, Z. Liu, L. Li and F. Yan, Metal-organic framework (MOF) facilitated highly stretchable and fatigue-resistant ionogels for recyclable sensors, *Mater. Horiz.*, 2022, **9**, 2881–2892.

27 K. Zhou, C. Zhang, Z. Xiong, H.-Y. Chen, T. Li, G. Ding, B. Yang, Q. Liao, Y. Zhou and S.-T. Han, Tactile Sensors: Template–Directed Growth of Hierarchical MOF Hybrid Arrays for Tactile Sensor, *Adv. Funct. Mater.*, 2020, **30**, 2001296.

28 J. Li, H. Jia, X. Ren, Y. Li, L. Liu, R. Feng, H. Ma and Q. Wei, Dumbbell Plate-Shaped AIEgen-Based Luminescent MOF with High Quantum Yield as Self-Enhanced ECL Tags: Mechanism Insights and Biosensing Application, *Small*, 2022, **18**, 2106567.

29 Y.-M. Wang, C. Liu, H. Zhi, X. Zhang, Y. Xu, Y. Wang, R. Yang and X.-B. Yin, Thiadiazole-functionalized metal-organic frameworks multifunction-architectonics for dual-target sensing of ethylamine and gossypol, *Chem. Eng. J.*, 2022, **441**, 136049.

30 S. Qin, M. Chen and L. Wu, An electrochemically deposited ordered hierarchical metal–organic framework-based dual-module sensor for decoding organic vapors, *J. Mater. Chem. A*, 2022, **10**, 21072–21079.

31 Y. Feng, Y. Xu, S. Liu, D. Wu, Z. Su, G. Chen, J. Liu and G. Li, Recent advances in enzyme immobilization based on novel porous framework materials and its applications in biosensing, *Coord. Chem. Rev.*, 2022, **459**, 214414.

32 W. Jia, R. Fan, J. Zhang, K. Zhu, S. Gai, Y. Yin and Y. Yang, Smart MOF-on-MOF Hydrogel as a Simple Rod-shaped Core for Visual Detection and Effective Removal of Pesticides, *Small*, 2022, **18**, 2201510.

33 J. Wang, D. Li, Y. Ye, Y. Qiu, J. Liu, L. Huang, B. Liang and B. Chen, A Fluorescent Metal-Organic Framework for Food Real-Time Visual Monitoring, *Adv. Mater.*, 2021, **33**, 2008020.

34 S.-L. Yang, G. Li, M.-Y. Guo, W.-S. Liu, R. Bu and E.-Q. Gao, Positive Cooperative Protonation of a Metal-Organic Framework: pH-Responsive Fluorescence and Proton Conduction, *J. Am. Chem. Soc.*, 2021, **143**, 8838–8848.

35 F. Walenszus, J. D. Evans, V. Bon, F. Schwotzer, I. Senkovska and S. Kaskel, Integration of Fluorescent Functionality into Pressure-Amplifying Metal-Organic Frameworks, *Chem. Mater.*, 2021, **33**, 7964–7971.

36 U. Kumar, A. Cuche, C. Girard, S. Viarbitskaya, F. Dell'Ova, R. Al Rafrafin, G. Colas des Francs, S. Bolisetty, R. Mezzenga, A. Bouhelier and E. Dujardin, Interconnect-Free Multibit Arithmetic and Logic Unit in a Single Reconfigurable 3 μm^2 Plasmonic Cavity, *ACS Nano*, 2021, **15**, 13351–13359.

37 W. Lee, M. Yu, D. Lim, T. Kang and Y. Song, Programmable DNA-Based Boolean Logic Microfluidic Processing Unit, *ACS Nano*, 2021, **15**, 11644–11654.

38 R. Maram, J. V. Howe, D. Kong, F. D. Ros, P. Guan, M. Galili, R. Morandotti, L. K. Oxenlowe and J. Azana, Frequency-domain ultrafast passive logic: NOT and XNOR gates, *Nat. Commun.*, 2020, **11**, 5839.

39 H. Chen, X. Xue, C. Liu, J. Fang, Z. Wang, J. Wang, D. W. Zhang, W. Hu and P. Zhou, Logic gates based on neuristors made from two-dimensional materials, *Nat. Electron.*, 2021, **4**, 399–404.

40 D. Li, Z. Li, P. Chen, L. Pi, H. Wang, X. Zhou and T. Zhai, Optical Logic Operation Encryption on ZnTe Flake, *Adv. Opt. Mater.*, 2022, **10**, 2200560.

41 X.-Y. Xu, X. Lian, J.-N. Hao, C. Zhang and B. Yan, A Double-Stimuli-Responsive Fluorescent Center for Monitoring of Food Spoilage based on Dye Covalently Modified EuMOFs: From Sensory Hydrogels to Logic Devices, *Adv. Mater.*, 2017, **29**, 1702298.

42 J. Dong, D. Zhao, Y. Lu and W.-Y. Sun, Photoluminescent metal–organic frameworks and their application for

This journal is © the Partner Organisations 2023

Inorg. Chem. Front., 2023, **10**, 1660–1670 | **1669**

sensing biomolecules, *J. Mater. Chem. A*, 2019, **7**, 22744–22767.

43 R. Goswami, S. C. Mandal, N. Seal, B. Pathak and S. Neogi, Antibiotic-triggered reversible luminescence switching in amine-grafted mixed-linker MOF: exceptional turn-on and ultrafast nanomolar detection of sulfadiazine and adenosine monophosphate with molecular keypad lock functionality, *J. Mater. Chem. A*, 2019, **7**, 19471–19484.

44 J. Z. Li, L. M. Dong, L. L. Zheng, W. L. Fu, J. J. Zhang, L. Zhang, Q. Hu, P. Chen, Z. F. Gao and F. Xia, Molecular Visual Sensing, Boolean Logic Computing, and Data Security Using a Droplet-Based Superwetting Paradigm, *ACS Appl. Mater. Interfaces*, 2022, **14**, 40447–40459.

45 X. Zheng, R. Fan, K. Xing, A. Wang, X. Du, P. Wang and Y. Yang, Dual-emissive nanocomposites based on Eu(III) functionalized Cu(I)-coordination polymer for ratiometric fluorescent sensing and integrating Boolean logic operations, *J. Mater. Chem. C*, 2018, **6**, 6229–6239.

46 J. Shi, M. Shen, W. Zhao, J. Liu, Z. Qu, M. Zhu, Z. Chen, P. Shi, Z. Zhang and S. S. Zhang, Ultrasensitive Dual-Signal Detection of Telomerase and MiR-21 Based on Boolean Logic Operations, *ACS Appl. Mater. Interfaces*, 2021, **13**, 51393–51402.

47 M. Chen, C. Wang, Z. Ding, H. Wang, Y. Wang and Z. Liu, A Molecular Logic Gate for Developing "AND" Logic Probes and the Application in Hepatopathy Differentiation, *ACS Cent. Sci.*, 2022, **8**, 837–844.

48 X. Ma, X. Chen, Y. Tang, R. Yan and P. Miao, Triple-Input Molecular AND Logic Gates for Sensitive Detection of Multiple miRNAs, *ACS Appl. Mater. Interfaces*, 2019, **11**, 41157–41164.

49 J. Othong, J. Boonmak, F. Kielar, S. Hadsadee, S. Jungsuttiwong and S. Youngme, Self-calibrating sensor with logic gate operation for anthrax biomarker based on nanoscaled bimetallic lanthanoid MOF, *Sens. Actuators, B*, 2020, **316**, 128156.

50 B. Hou, L. Zhou, H. Wang, M. Saeed, D. Wang, Z. Xu, Y. Li and H. Yu, Engineering Stimuli-Activatable Boolean Logic Prodrug Nanoparticles for Combination Cancer Immunotherapy, *Adv. Mater.*, 2020, **32**, 1907210.

51 Z.-H. Jiao, X.-L. Jiang, S.-L. Hou, M.-H. Tang and B. Zhao, Highly Sensitive and Selective Luminescence Sensor Based on Two-Fold Interpenetrated MOFs for Detecting Glutamate in Serum, *Inorg. Chem.*, 2020, **59**, 2171–2177.

52 M.-H. Tang, Y. Shi, X.-L. Jiang, H. Xu, Y. Ma and B. Zhao, A high sensitivity luminescent sensor for the stress biomarker cortisol using four-fold interpenetrated europium–organic frameworks integrated with logic gates, *J. Mater. Chem. C*, 2021, **9**, 9643–9649.

53 J.-N. Hao and Y. Li, Concurrent Modulation of Competitive Mechanisms to Design Stimuli–Responsive Ln–MOFs: A Light–Operated Dual–Mode Assay for Oxidative DNA Damage, *Adv. Funct. Mater.*, 2019, **29**, 1903058.

54 X. Liu, B. Liu, G. Li and Y. Liu, Two anthracene-based metal–organic frameworks for highly effective photodegradation and luminescent detection in water, *J. Mater. Chem. A*, 2018, **6**, 17177–17185.